

# A computational study of axial dispersion in segmented gas-liquid flow

Metin Muradoglu<sup>a)</sup>

*Department of Mechanical Engineering, Koc University, Rumelifeneri Yolu, Sariyer 34450 Istanbul, Turkey*

Axel Günther<sup>b)</sup>

*Department of Mechanical & Industrial Engineering and Institute of Biomaterials and Biomedical Engineering, University of Toronto, 5 King's College Road, Toronto, Ontario, Canada M5S 3G8*

Howard A. Stone<sup>c)</sup>

*School of Engineering and Applied Sciences, Harvard University, Cambridge, Massachusetts 02138, USA*

(Received 4 January 2007; accepted 24 May 2007; published online 25 July 2007)

Axial dispersion of a tracer in a two-dimensional gas-liquid flow is studied computationally using a finite-volume/front-tracking method. The effects of Peclet number, capillary number, and segment size are examined. At low Peclet numbers, the axial dispersion is mainly controlled by the convection through the liquid films between the bubbles and channel walls. In this regime, the computational results are found to be in a very good agreement with the existing model due to Pedersen and Horvath [Ind. Eng. Chem. Fundam. **20**, 181 (1981)]. At high Peclet numbers, the axial dispersion is mainly controlled by the molecular diffusion, with some convective enhancement. In this regime, a new model is proposed and found to agree well with the computational results. These Peclet number regimes are shown to persist for different slug lengths. The axial dispersion is found to depend weakly on the capillary number in the diffusion-controlled regime. Finally, computational simulations are performed for the cases of six bubbles to mimic bubble trains, and results are compared with the theoretical models. © 2007 American Institute of Physics.

[DOI: 10.1063/1.2750295]

## I. INTRODUCTION

Segmented gas-liquid flows are of importance in a variety of engineering processes such as two-phase catalytic monolith reactors,<sup>1–4</sup> polymer blow molding, enhanced oil recovery,<sup>5</sup> continuous-flow analysis of biological or chemical samples (e.g., AutoAnalyzer),<sup>6–8</sup> and, more recently, microfluidics applications.<sup>9</sup> Not surprisingly, the fluid dynamics of these flows have been studied extensively, with two widely cited early references: Taylor<sup>10</sup> and Bretherton.<sup>11</sup> Studies of mass transfer have focused on experiments and simplified models. In this paper, we report on a numerical study that accounts for both the fluid dynamics and convective-diffusive mass transfer. The understanding from these detailed simulations then motivates an improved model of the basic transport processes at the scale of the bubble.

In the case considered here, a wetting continuous-phase liquid flowing through a capillary tube is segmented by equally sized and spaced gas bubbles of an equivalent diameter larger than the channel size as sketched in Fig. 1. The bubbles completely fill the channel cross section except for thin liquid films that separate them from the channel wall. The low-Reynolds-number flow field inside the liquid slug between two bubbles is significantly modified compared to

the flow of a single-phase liquid and it can be characterized by the capillary and Peclet numbers defined as  $Ca = \mu U_b / \sigma$  and  $Pe = U_b w / D$ , respectively, where  $\mu$ ,  $U_b$ ,  $\sigma$ ,  $w$ , and  $D$  are the liquid viscosity, the bubble velocity, surface tension, the width of the channel, and molecular diffusivity of solute in the liquid, respectively. Note that the influence of the Reynolds number is typically weak in such flows.<sup>12–14</sup> When the capillary number is small, i.e.,  $Ca \ll 1$ , the bubbles adopt a characteristic capsular shape and, relative to a coordinate system moving with the bubbles, create a toroidal rotating vortical flow pattern in the liquid slugs. This convective flow pattern offers distinct advantages over the single-phase liquid flow. First, the recirculation significantly enhances mixing in the liquid slugs leading to augmented heat and mass transfer in the radial direction; second, axial dispersion is greatly reduced when segmented flow occurs instead of homogeneous laminar flow.<sup>15</sup> The combination of enhanced heat and mass transfer in the radial direction and low dispersion in the axial direction makes the segmented flow suitable for applications in two-phase systems involving mass transfer, gas-liquid or wall-liquid-solid chemical reactions, or reactions in single-phase systems that otherwise suffer from excessive back mixing.<sup>16</sup>

The liquid films between the gas bubbles and the channel wall provide the only means of communication between two successive liquid slugs. In the limit of small capillary number, i.e.,  $Ca \ll 1$ , Bretherton<sup>11</sup> showed that the bubble moves a little faster than the mean speed of the liquid and the film thickness is given by  $h/\ell = c_1 Ca^{2/3}$ , where  $\ell$  is the characteristic channel size and  $c_1$  is a constant of order of unity.

<sup>a)</sup> Author to whom correspondence should be addressed. Telephone: +90 (212) 338 14 73. Fax: +90 (212) 338 15 48. Electronic mail: mmuradoglu@ku.edu.tr

<sup>b)</sup> Telephone: +1 (416) 978-1282. Fax: +1 (416) 978-7753. Electronic mail: axel.guenther@utoronto.ca

<sup>c)</sup> Telephone: +1 (617) 495-3599. Fax: +1 (617) 495-9837. Electronic mail: has@deas.harvard.edu

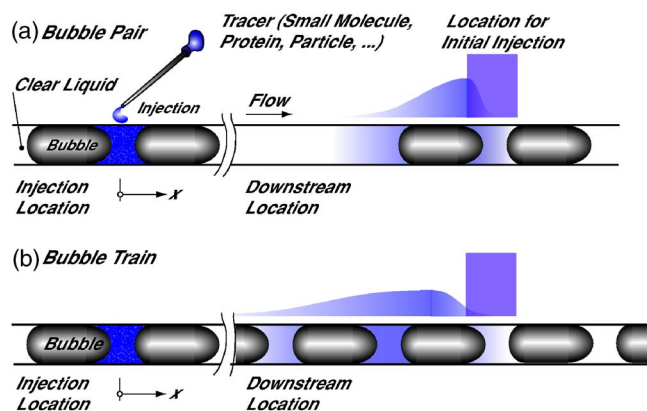


FIG. 1. (Color online) Schematic illustration of a two-bubble system (top figure) and a bubble train (lower figure).

In the majority of applications of practical importance, the film thickness is only a fraction of the characteristic channel size.

The axial dispersion in gas-liquid segmented flow is a result of mass transfer from the bulk fluid to the slow moving film region by a combined effect of molecular diffusion and convection due to recirculation in the liquid slugs. The effect of molecular diffusion is characterized by the Peclet number. Although axial dispersion is much reduced in the segmented gas-liquid flow compared to an equivalent single-phase system, because of the nearly stagnant film region there may still be significant backmixing especially in the case of small Peclet numbers and for larger capillary numbers where films are thicker. In particular, this backmixing may significantly deteriorate the performance of monolith reactors.<sup>17,18</sup> It is therefore of fundamental importance to understand and control the axial dispersion in gas-liquid segmented systems.

Recent studies of the gas-liquid segmented flow have been motivated primarily by applications in catalytic monolith reactors<sup>4,18–20</sup> and mixing enhancement combined with chemical and material synthesis in microfluidic systems.<sup>9,21,22</sup> In particular, Pedersen and Horvath<sup>15</sup> developed a model based on a two-region description of the segmented flow: mass transfer from the recirculating bulk liquid region to the film region was modeled through an adjustable mass transfer coefficient and a perfect mixing was assumed in both regions. Bercic and Pintar<sup>1</sup> numerically modeled the effects of gas bubbles and liquid slug length on the axial mass transfer in the segmented flow and found that the mass transfer is mainly determined by the slug length and velocity. Thulasidas *et al.*<sup>19</sup> also divided the liquid slugs into the recirculating and film regions but solved a one-dimensional diffusion equation in the radial direction to account for mass transfer by molecular diffusion. Although they ignored the effects of convection in the recirculating region, they showed a good agreement between their mathematical model and experimental results. More recently, Salman *et al.*<sup>23,24</sup> proposed a model based on a one-dimensional convection-diffusion equation. They found that the axial dispersion is in general low and increases with increasing capillary number and slug and bubble lengths. As a final remark, Trachsel *et al.*<sup>25</sup> recently developed an experimental technique for on-chip dis-

persion measurements in gas-liquid segmented flows and found that the variance of the residence time distribution (RTD) was significantly smaller for segmented gas-liquid flows than the single-phase flow at similar conditions.

In the present paper, we study the axial dispersion in a gas-liquid segmented flow using a finite-volume/front-tracking method<sup>26</sup> in a two-dimensional setting. Passive tracer particles are used to visualize and quantify the mass transfer. Molecular diffusion is modeled by a random walk of the tracer particles. Computations are performed to show the effects of Peclet number, capillary number, and slug length on the axial dispersion in the segmented flow. Based on the results from these simulations, a simple analytical model is proposed and compared with the numerical results. The present model is similar to the earlier models in the sense that it divides the liquid slugs into recirculating and film regions. However, the new model not only accounts for the molecular diffusion in the radial direction, but it also accounts for the effects of the convection by the nonuniform velocity profile in the liquid segment. Reasonably good agreement is found between the analytical model and computational results at high Peclet numbers, i.e.,  $Pe > 10^3$ . It is also found that the computational results are in very good agreement with Pedersen and Horvath's model<sup>15</sup> in the limit of perfect mixing in the slug, i.e., in the limit as  $Pe \rightarrow 0$ . Finally simulations are performed for a six-bubble system to mimic bubble trains and computational results are compared with Pedersen and Horvath's model<sup>15</sup> again in the convection-controlled regime.

The paper is organized as follows. The mathematical formulation and numerical method are briefly summarized in the next section and details are provided in the Appendix. The physical problem is described in Sec. III. The results are presented and discussed in Sec. IV and conclusions are drawn in Sec. V.

## II. FORMULATION AND NUMERICAL METHOD

The governing equations and numerical method are briefly described in this section and details are provided in the Appendix. The numerical simulations are performed using the finite-volume/front-tracking method developed by Muradoglu and Kayaalp.<sup>26</sup> In this method, a single set of flow equations is written for the entire computational domain and different phases are treated with variable material properties.<sup>27,28</sup> The effects of surface tension are treated as body forces and added to the momentum equations as delta functions at the phase boundaries. As discussed in the Appendix, the resulting system of the equations is in the same form as the standard incompressible flow equations so that it can be solved by virtually any standard flow solver developed for single-phase flow simulations.

In the present study, the front-tracking method developed by Unverdi and Tryggvason<sup>28</sup> is combined with a finite-volume solver. The continuity and momentum equations are solved on a curvilinear grid using a finite-volume method. The spatial derivatives are approximated by a finite-volume method that is equivalent to second-order finite differences on a regular mesh. A dual (or pseudo) time-stepping

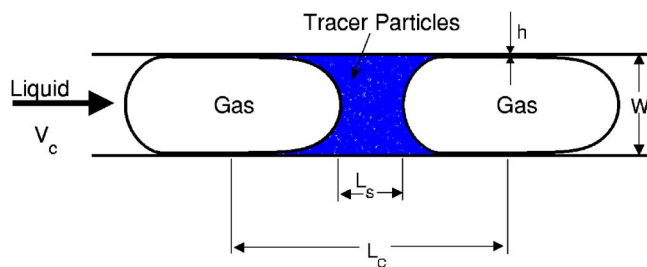


FIG. 2. (Color online) A schematic illustration of the portion of a two-dimensional channel containing two bubbles and one liquid segment. A large number of tracer particles are distributed at random in the liquid segment after gas bubbles reach their steady shapes.

method is employed to achieve time accuracy and an alternating direction implicit (ADI) method is used to perform integration in pseudo time. Fourth-order numerical dissipation terms are added to the discrete version of the flow equations to prevent the odd-even decoupling. Preconditioning, local time-stepping, and multigrid methods are used to accelerate the convergence rate of the ADI method in the pseudo time. Details of the FV method can be found in Refs. 26 and 29.

A large number of passive tracer particles are used to visualize and quantify mixing in the continuous fluid. The molecular mixing is modeled by a random walk of tracer particles, which are advected with the local fluid velocity interpolated from the Eulerian grid. The details of the governing equations for the evolution of the tracer particles and the numerical solution procedure are provided in the Appendix. The result of this approach is a full numerical solution of the Navier-Stokes equations and the corresponding convective-diffusive mass transfer equation, while simultaneously determining the bubble shapes.

### III. PROBLEM STATEMENT

The axial dispersion in gas-liquid segmented flow is studied in a two-dimensional setting to facilitate extensive computational simulations. We consider a long straight channel of length  $L$  and width  $w$ . A portion of the channel that contains gas bubbles and a liquid segment is sketched in Fig. 2. The flow rate is specified at the inlet assuming a fully developed velocity profile with an average velocity of  $V_c$ . A steady single-phase flow is computed first using the liquid properties and is then used as the initial conditions. The bubbles are instantaneously placed in the channel close to the entrance section. The bubbles are much longer than the channel width and are initialized with an approximate shape consisting of a straight middle and semicircular front and back sections.

The distance between the centers of gas bubbles is denoted by  $L_c$  and the equivalent slug length  $L_s$  is defined as  $L_s = A_s/w$ , where  $A_s$  is the area of the liquid slug. The properties of gas bubble and liquid are denoted by subscripts  $b$  and  $o$ , respectively. The governing nondimensional numbers are defined as the channel Reynolds number  $Re = \rho_o V_c w / \mu_o$ , the capillary number  $Ca = \mu_o U_b / \sigma$ , the Peclet number  $Pe = U_b w / D$ , viscosity ratio  $\lambda = \mu_b / \mu_o$ , and the density ratio

$\gamma = \rho_b / \rho_o$ . Also, the normalized initial separation between the bubbles is denoted by  $\Lambda = L_{is}/w$ , where  $L_{is}$  is defined as the minimum distance between two successive bubbles when they are initialized in the channel. All the computations are performed at  $Re=0.64$ ,  $\lambda=0.1$ , and  $\gamma=0.1$ . The film thickness  $h$  between the bubbles and the channel walls is initially much smaller than the value obtained from the theoretical estimate<sup>12,14</sup>

$$\frac{h}{w} = \frac{1.3375Ca^{2/3}}{1 + 3.344Ca^{2/3}}. \quad (1)$$

Subsequently, the film thickness relaxes to the value given by Eq. (1) as the bubbles approach their steady shapes. The tracer particles are introduced when the bubbles reach their steady shapes. The tracers are initially distributed at random in the liquid slug between the centroids of the leading two bubbles as shown in Fig. 2.

The average tracer concentration in the  $n$ th slug is defined as

$$\langle C \rangle_n = \frac{N_n}{A_{sn}}, \quad (2)$$

where  $N_n$  is the total number of particles and  $A_{sn}$  is the area of the liquid slug. Since  $A_{sn}$  remains essentially constant after the initial transient, the concentration is computed simply as the total number of particles in the slug in all the results presented here. The results are nondimensionalized using the length scale  $\mathcal{L} = w$ , the velocity scale  $\mathcal{U} = U_b$ , and the time scale  $\mathcal{T} = w/U_b$ , and the nondimensional quantities are denoted by superscript “\*.”

Extensive numerical simulations are performed for a two-bubble and a six-bubble systems using nonuniform Cartesian grids. The grids are stretched to better resolve the thin liquid films adjacent to the channel walls, and care is taken to have at least five grid points within the film regions in all the results presented in this paper. Since extensive grid convergence and other numerical accuracy tests have been performed earlier for this kind of two-phase flow problem,<sup>13,14</sup> a similar study is not repeated here and instead the numerical accuracy is assessed by comparing the film thickness with Eq. (1). The difference between the computed film thickness and Eq. (1) is found to be less than 6% in all the results presented here.

### IV. RESULTS AND DISCUSSION

#### A. Two-bubble system

Computations are first performed for a two-bubble system and effects of the governing nondimensional numbers on the axial dispersion are examined. For this purpose, the channel length is set to  $L=30w$  and the computational domain is resolved by a  $768 \times 64$  nonuniform Cartesian grid. About 30000 tracer particles are used in the simulations of transport for the two-bubble system.

First, the effects of the Peclet number on the axial dispersion are examined. For this purpose, the Peclet number is varied in the range between  $Pe=10$  and  $Pe \rightarrow \infty$  while keeping the other nondimensional numbers fixed at  $Ca=0.01$ ,



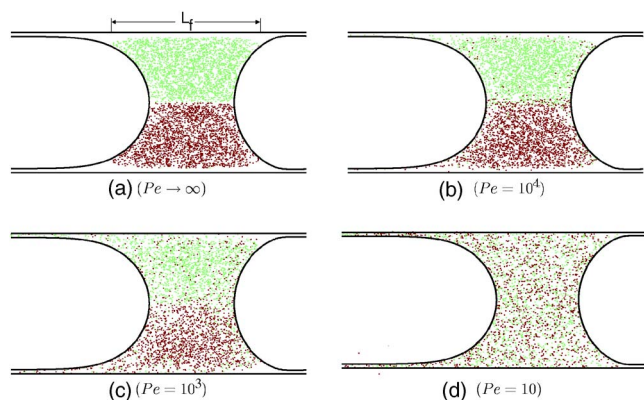


FIG. 3. (Color online) Scatter plots of tracer particles for various Peclet numbers at nondimensional time  $t^* = 11.2$ . Different colors are used for the particles initially located in the lower and upper portions of the liquid segment to show mixing patterns ( $Ca = 0.01$ ,  $Re = 0.64$ ).

$\Lambda = 0.75$ ,  $Re = 0.64$ ,  $\lambda = 0.1$ , and  $\gamma = 0.1$ . Note that, for the case of quantum dot synthesis in microchannels,<sup>22</sup> the Peclet number approximately ranges between  $Pe = 2000$  and  $6000$ . The viscosity ratio,  $\lambda = 0.1$ , is larger than typical values used in microfluidic applications, i.e.,  $\lambda \sim 0.001$  for ethanol/air or water/air systems. However, the effects of viscosity ratio are expected to be small when  $\lambda \leq 0.1$  for these kind of problems as discussed by Muradoglu and Stone.<sup>13,14</sup> Since the numerical method is fully implicit in time, the time step is solely determined by the accuracy considerations. The nondimensional time step is set to  $\Delta t^* = 0.005$  for  $Pe \geq 100$  and is reduced to  $\Delta t^* = 0.002$  for  $Pe \leq 50$  to keep the numerical error small. The time accuracy was tested for two extreme cases (not presented here) of  $Pe = 10$  and  $Pe \rightarrow \infty$  (by setting  $D = 0$ ), and in both cases it is found that the time-stepping error was negligible.

The scatter plots of tracer particles in the liquid slug are shown in Fig. 3 for  $Pe = 10, 10^3, 10^4$ , and  $\infty$  at nondimensional time  $t^* = 11.2$  to provide a visual aid to illustrate the effects of Peclet number on the mixing and the diminished concentration in the liquid plug as a consequence of fluid draining through the liquid films. Note that the tracers that initially occupy the upper and lower halves of the liquid plug are colored differently in order to visualize the mixing in the liquid segment. As can be seen, all the tracer particles that were initialized in the recirculating region are trapped in the liquid region in the absence of molecular diffusion, i.e.,  $Pe \rightarrow \infty$ , and mixing increases as  $Pe$  decreases. Note that the case of  $Pe \rightarrow \infty$  is also useful to identify the recirculating liquid and the film regions.

These results are quantified in Fig. 4, where the average tracer concentration in the liquid slug is plotted as a function of the nondimensional time for various Peclet numbers. In this figure, the average concentrations are normalized by the initial concentration in the slug,  $\langle C \rangle_i$ . After a transient period, the concentration remains constant in the case of  $Pe \rightarrow \infty$ ; during the transient, the concentration is reduced simply because the tracer particles originally in the film region are convected downstream (relative to a reference frame fixed to a bubble) and in the absence of diffusion no additional par-

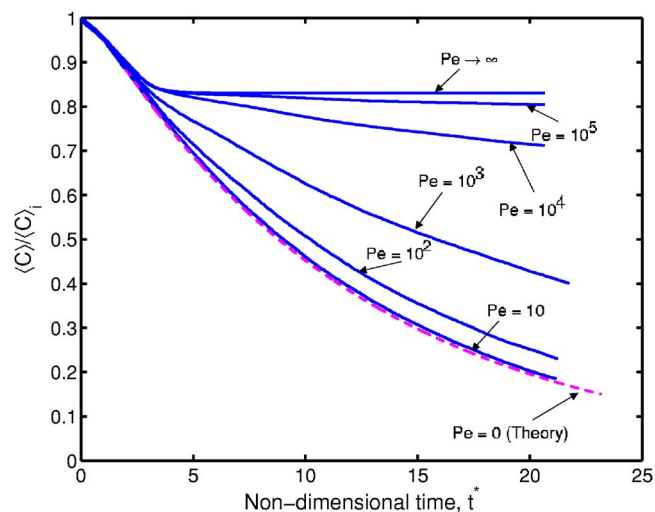


FIG. 4. (Color online) Evolution of tracer concentration in the liquid segment as a function of nondimensional time for various Peclet numbers ranging between  $Pe = 10$  and  $Pe \rightarrow \infty$ . The dashed curve indicates the theoretical result as  $Pe \rightarrow 0$ .

ticles migrate to the wall region. On the other hand, at finite Peclet numbers, the average concentration decreases monotonically as time progresses. Figure 4 also illustrates that the axial dispersion increases as the Peclet number decreases and for  $Pe = 10$  approaches the predictions of an asymptotic regime as  $Pe \rightarrow 0$ . As shown by Pedersen and Horvath,<sup>15</sup> for  $Pe \rightarrow 0$ , the average concentration in the liquid slug approaches a convection-controlled regime and is described by

$$\frac{\langle C \rangle}{\langle C \rangle_i} = e^{-\alpha t^*}, \quad (3)$$

where  $\alpha = 2hw/A_s$ . Equation (3) is plotted as a dashed curve in Fig. 4. Note that the area of the slug  $A_s$  is computed approximately from the snapshot shown in Fig. 3(a). As can be seen in Fig. 4, the theoretical result is in good agreement with the computational result obtained for  $Pe = 10$ . We thus see that the low Peclet number theory is actually applicable at moderate Peclet numbers ( $Pe = 10$ ).

To better understand the finite Peclet number effects on the axial dispersion, it is necessary to describe transport into the regions near the wall. Thus, we consider a model of the liquid slug flow near the wall, as sketched in Fig. 5. In the reference frame moving with the bubbles, the flow is assumed to be one-dimensional in the liquid slug and the velocity varies linearly with position normal to the wall as sketched in Fig. 5(b). In the local coordinate system in Fig. 5(b), the velocity profile is approximated by

$$u = U_0 + Gy, \quad (4)$$

where  $U_0 = [h_b/(h_b + h_f)]U_b$  and the shear rate  $G = U_b/(h_b + h_f)$ . The length scales  $h_f$  and  $h_b$  can be approximated as the liquid film thickness and the distance between the center of the vortex in the slug and the film region, respectively. Thus, in the steady state, the tracer concentration  $C(x, y)$  in the near wall region is governed by

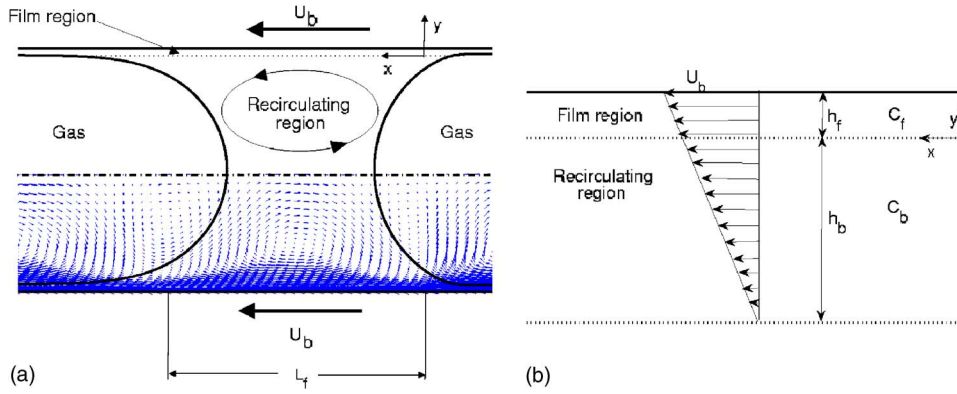


FIG. 5. (Color online) The schematic illustration of the model based on the decomposition of the liquid slug into the film and recirculating regions. (a) The film and recirculating regions. The velocity vectors plotted in the lower portion of the channel are taken from our computational simulations. (b) The idealized velocity profile near the film regions.

$$(U_0 + Gy) \frac{\partial C}{\partial x} = D \frac{\partial^2 C}{\partial y^2}, \quad (5)$$

where we have assumed that convective transport dominates diffusion in the  $x$  direction. Assuming that the concentration boundary layer remains thinner than the liquid films and the concentration at the center of the recirculating liquid region is approximately equal to the average concentration in the plug, the boundary conditions are specified as

$$C|_{y=-h_b} = C_b, \quad C|_{y \rightarrow \infty} = C_f, \quad C|_{x=0} = \begin{cases} C_f & \text{if } y \geq 0, \\ C_b & \text{if } y < 0, \end{cases} \quad (6)$$

where  $C_f$  and  $C_b$  are the concentration in the film region at  $x=0$  and the average concentration in the recirculating liquid region, respectively. Letting  $z = U_0 + Gy$ , Eq. (5) becomes

$$z \frac{\partial C}{\partial x} = DG^2 \frac{\partial^2 C}{\partial z^2}. \quad (7)$$

Equation (7) is in the same form as the Leveque problem<sup>30,31</sup> and admits a similarity solution. Let

$$\eta = \frac{z}{(3DG^2x)^{1/3}}, \quad (8)$$

so Eq. (7) becomes

$$\frac{d^2 C}{d\eta^2} + \eta^2 \frac{dC}{d\eta} = 0, \quad (9)$$

which can be integrated to yield

$$C = c_1 + c_2 \int_0^\eta e^{-1/3 \xi^3} d\xi. \quad (10)$$

In Eq. (10),  $c_1$  and  $c_2$  are the integration constants that can be determined from the boundary conditions as

$$c_1 = C_b, \quad c_2 = \frac{3^{2/3}(C_f - C_b)}{\Gamma(1/3)}, \quad (11)$$

where  $\Gamma$  is the Gamma function. The flux of tracer particles,  $q$ , from the recirculating bulk region to the film region (i.e., across  $y=0$ ), accounting for the films on the two sides, is computed as

$$q = 2 \int_0^{L_f} \left( -D \frac{\partial C}{\partial y} \right)_{y=0} dx, \\ = \frac{2U_0^2(C_b - C_f)}{3\Gamma(1/3)G} \int_\beta^\infty t^{-5/3} e^{-t} dt, \quad (12)$$

where  $L_f$  is the length of the boundary between the film and recirculating regions [see Fig. 3(a)] and

$$\beta = \frac{U_0^3}{9DG^2L_f} = \frac{h_b^3}{9D(h_b + h_f)} \frac{U_b}{L_f}. \quad (13)$$

Equation (12) gives the flux of tracer particles from the recirculating liquid region to the wall region and these particles are subsequently lost through the films. Thus, similar to the convection-controlled regime<sup>15</sup> [see also Eq. (3)], one can easily show that the average concentration in the liquid slug evolves according to

$$\frac{\langle C \rangle}{\langle C \rangle_i} = e^{-\alpha_1 t^*}, \quad (14)$$

where the decay rate  $\alpha_1$  is given by

$$\alpha_1 = \frac{w}{U_b A_s (C_b - C_f)} q = \frac{2wU_0^2}{3\Gamma(1/3)U_b A_s G} \int_\beta^\infty t^{-5/3} e^{-t} dt. \quad (15)$$

Equation (15) is complicated and difficult to interpret. However, the decay rate approaches asymptotically to

$$\alpha_1 = \begin{cases} 1.46 \text{Pe}^{-2/3} \text{Ca}^{-2/9} \left( \frac{L_f}{L_s} \right)^{2/3} \left( \frac{w}{L_s} \right)^{1/3} & \text{as } h_b/h_f \rightarrow 0, \\ 1.13 \text{Pe}^{-1/2} \left( \frac{w}{L_s} \right)^{1/2} & \text{as } h_b/h_f \rightarrow \infty, \end{cases} \quad (16)$$

where the width of the film region has been approximated using the Bretherton's approximation  $h_f = 1.3375 w \text{Ca}^{2/3}$ .<sup>11</sup> The length scale  $L_f$  can be approximated as the length of the interface between the bulk and film regions as shown in Fig. 3(a). Therefore, it is reasonable to assume that the decay rate scales as  $\alpha_1 \sim \text{Pe}^{-n}$ , where  $1/2 \leq n \leq 2/3$ . By expanding Eq. (14) into a Taylor's series, we obtain

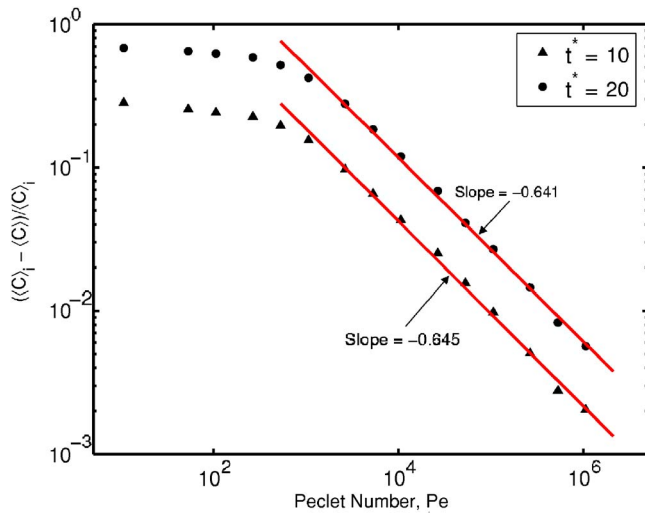


FIG. 6. (Color online) Variation of the average tracer concentration as a function of the Peclet number for a small liquid segment, i.e.,  $\Lambda=0.75$ , at nondimensional times  $t^*=10$  and 20. ( $Ca=0.01$  and  $Re=0.64$ .)

$$\frac{\langle C \rangle - \langle C \rangle_i}{\langle C \rangle_i} \approx Pe^{-n} t^{*} + O(Pe^{-2n} t^{*2}). \quad (17)$$

This power-law scaling is verified for  $Pe > 10^3$  in Fig. 6, where the relative average concentration is plotted as a function of Peclet number at time  $t^*=10$  and 20. The results clearly show the scaling given by Eq. (17) and also indicate three different regimes, namely the convection-controlled regime when  $Pe > 10^3$ , the diffusion-controlled regime when  $Pe < 10^2$ , and transition regime when  $10^2 \leq Pe \leq 10^3$ . A similar behavior and scaling are also observed for a larger liquid slug size, i.e.,  $\Lambda=1.5$ , as shown in Fig. 7. We thus see that a model of boundary-layer mass transfer predicts the Peclet number dependence very well in the diffusion-controlled regime.

However, the numerical value of the exponent  $n \approx 0.65$  corresponds to the limiting case of  $h_b/h_f \rightarrow 0$ , which is

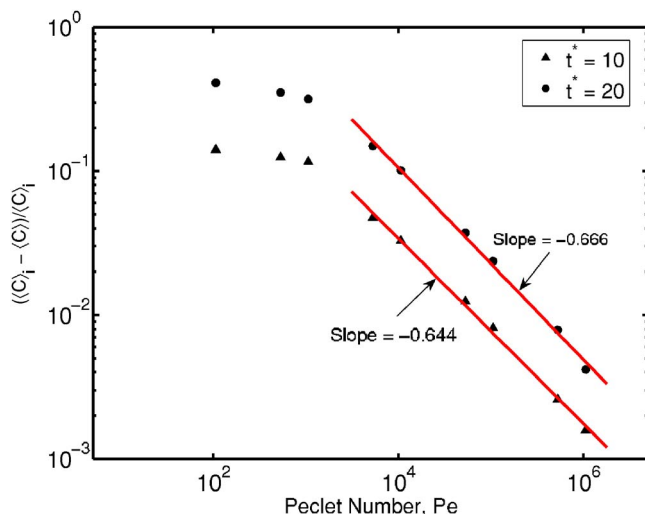


FIG. 7. (Color online) Variation of the average tracer concentration as a function of the Peclet number for a large liquid segment, i.e.,  $\Lambda=1.5$ , at nondimensional times  $t^*=10$  and 20. ( $Ca=0.01$  and  $Re=0.64$ .)

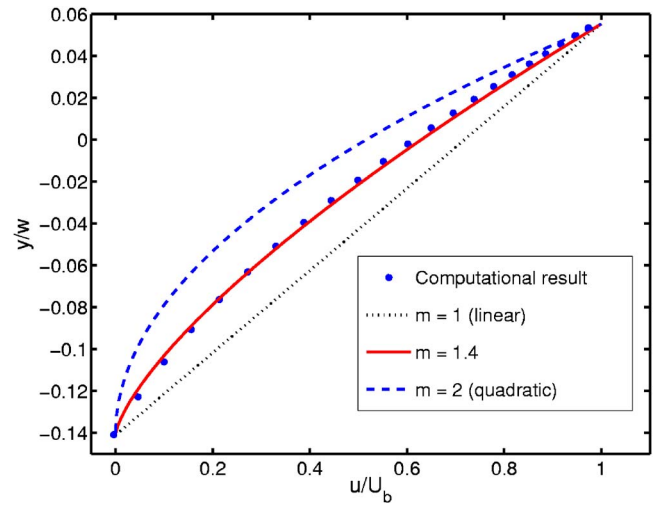


FIG. 8. (Color online) A typical velocity profile at the center of the liquid slug in the near wall region. The coordinate system is the same as that in Fig. 5. The symbols denote the computational result and lines denote different power-law approximations in the form  $u/U_b = (h_b/h_b + h_f)^m (1 + y/h_b)^m$ .

clearly not the case since the center of the recirculation zone is always below the boundary between the film and bulk regions. This may be explained by the fact that the velocity profile is not really linear but it is rather in between linear and quadratic, as shown in Fig. 8. In this figure, the velocity profile at the center of the liquid slug is plotted near the wall region in the same coordinate system as defined in Fig. 5 and a general power-law velocity profile is defined as

$$\frac{u}{U_b} = \left( \frac{h_b}{h_b + h_f} \right)^m \left( 1 + \frac{y}{h_b} \right)^m, \quad (18)$$

where  $m$  is a real number. A similarity solution can be found for this general power-law velocity profile in the same way as discussed above for the linear velocity profile. In particular, the similarity solution yields  $n=1/2$  and  $n=\frac{m+1}{m+2}$  for the cases of  $h_b/h_f \rightarrow \infty$  and  $h_b/h_f \rightarrow 0$ , respectively. As can be seen in Fig. 8,  $m=1.4$  yields a very good approximation to the computational velocity profile. Therefore, it is reasonable to expect that  $0.5 \leq n \leq 0.71$ , which agrees well with the computational value of  $n \approx 0.65$ . To the best of our knowledge, no model has been offered until this time for the Peclet number dependence of dispersion in the segmented systems.

We next examine the effects of capillary number on the axial dispersion. The simple model given above predicts a very weak dependence of axial dispersion on the capillary number in the diffusion-controlled limit. However, in the convection-controlled limit, axial dispersion depends strongly on the capillary number since the film thickness increases rapidly with increasing capillary number, as can be seen in Eq. (1). This effect is verified in Fig. 9, where the average concentration in the slug is plotted as a function of nondimensional time for  $Ca=0.02$ , 0.01, and 0.005, and for  $Pe=10^2$  and  $10^4$ . As can be seen in this figure, there is a strong dependence of average concentration on capillary number in the convection-controlled regime (e.g.,  $Pe=10^2$ ) while in the diffusion-controlled regime (e.g.,  $Pe=10^4$ ), after a transient period of time, the decay rates are about the same

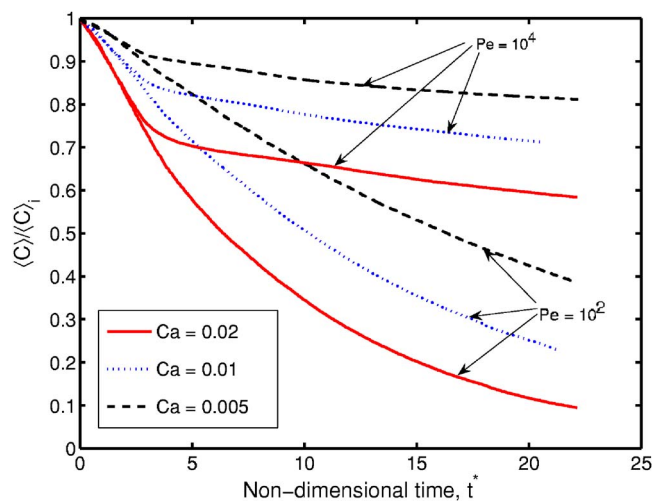


FIG. 9. (Color online) Effects of the capillary number on evolution of the average tracer concentration in the liquid segment as a function of non-dimensional time for  $Pe=10^2$  and  $10^4$ . ( $Ca=0.01$  and  $Re=0.64$ .)

for all capillary numbers, indicating a very weak dependence of the average concentration on the capillary number as predicted by the model [see, e.g., Eq. (16)].

## B. Bubble trains

We now consider a six-bubble system to mimic bubble trains widely used in monolith reactors<sup>3</sup> and micromixers.<sup>9,21</sup> In this case, the channel length is  $L=60w$  and the computational domain is resolved by a  $1200 \times 64$  nonuniform grid. The liquid slug between the first two leading bubbles is labeled by “0” and the slugs following the zeroth slug are labeled by “1,” “2,” “3,” and “4,” respectively. About  $10^5$  tracer particles are introduced in the zeroth liquid slug when the bubbles reach their steady shapes in the same way as the two-bubble system. Not surprisingly, the simulations for bubble trains take much longer than for the two-bubble problems. The Reynolds number, the capillary number, the viscosity ratio, and the density ratio are fixed at  $Re=0.64$ ,  $Ca=0.01$ ,  $\lambda=0.1$ , and  $\gamma=0.1$ , respectively. The average

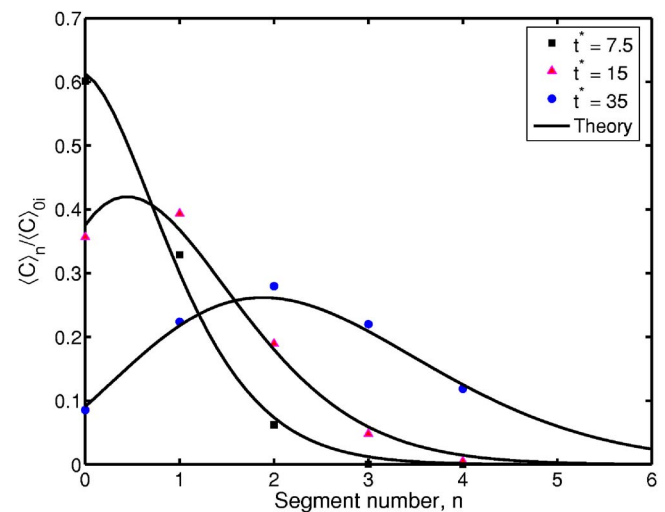


FIG. 11. (Color online) Average tracer concentration as a function of segment number at various time frames for  $Pe=10^2$ . The symbols are the numerical simulations and solid lines are theoretical results. ( $Ca=0.01$ ,  $\Lambda=0.75$ , and  $Re=0.64$ .)

tracer concentration in each slug is computed in the same way as the two-bubble case and the average concentration in the  $n$ th slug is denoted by  $\langle C \rangle_n$ . These mean concentrations evolve in time.

The time evolution of average tracer concentrations in the liquid slugs is plotted in Fig. 10(a) and 10(b) for  $Pe=10^2$  and  $10^4$ , respectively, as typical examples for convection-controlled and diffusion-controlled regimes. As discussed by Pedersen and Horvath,<sup>15</sup> in the convection-controlled regime, i.e., as  $Pe \rightarrow 0$ , the normalized concentration in the  $n$ th segment evolves according to

$$\frac{\langle C \rangle_n}{\langle C \rangle_{0i}} = \frac{(\alpha t^*)^n}{n!} e^{-\alpha t^*}, \quad (19)$$

where  $\alpha=2hw/A_s$  as before and  $\langle C \rangle_{0i}$  is the initial average concentration in the zeroth segment. This theoretical result is verified in Fig. 11, where the average concentration in each segment is plotted as a function of the segment number at

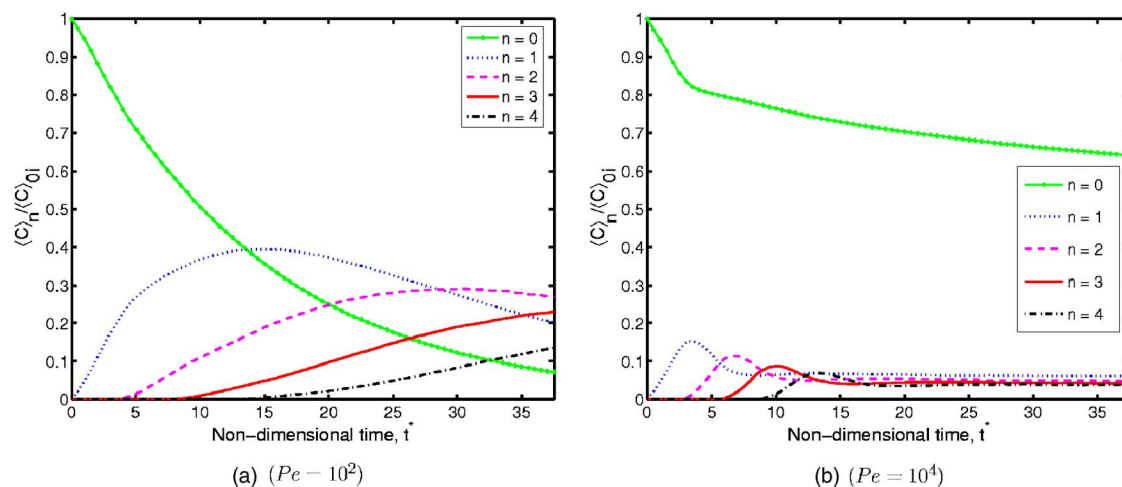


FIG. 10. (Color online) Time evolution of average tracer concentration in each liquid segment in a bubble-train flow involving six bubbles. ( $Ca=0.01$ ,  $\Lambda=0.75$ , and  $Re=0.64$ .)



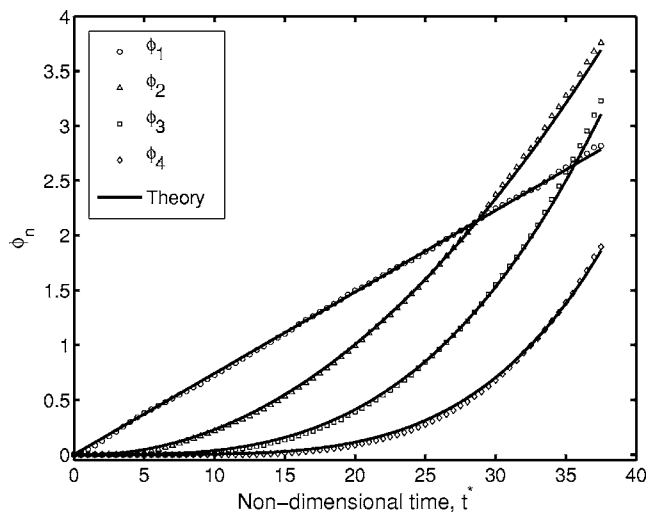


FIG. 12. Time evolution of relative average tracer concentration in each liquid segment in the bubble-train flow for  $Pe=10^2$ . The symbols are the numerical simulations and solid lines are the theoretical results. ( $Ca=0.01$ ,  $\Lambda=0.75$ , and  $Re=0.64$ .)

time frames  $t^*=7.5, 15$ , and  $35$ , and is compared with the theoretical result given by Eq. (19). Note that  $n!$  in Eq. (19) is replaced by the Gamma function using the relation  $n!=\Gamma(n+1)$  to obtain a continuous variation. As can be seen in this figure, there is good agreement between the computational and theoretical results. The small discrepancies between the numerical and theoretical results are partly attributed to the finite value of the Peclet number used in the simulations.

The relative concentration in the  $n$ th segment is given by

$$\phi_n(t) \equiv \frac{\langle C \rangle_n}{\langle C \rangle_0} = \frac{(\alpha t^*)^n}{n!}, \quad (20)$$

where Eq. (19) has been used. This result is verified in Fig. 12, where the relative concentration in each segment is plotted as a function of nondimensional time and is compared with the theoretical result. Note that, since Eq. (20) is valid only in a steady state, the transient time needed for particles to reach each segment is taken into account in Fig. 12 by simply starting the time after the transient period for each segment. In the present results, the transient period of time for the  $n$ th segment is taken as  $T_n^*=nT_{\text{shift}}^*$ , where  $T_{\text{shift}}^*=0.9$ . As can be seen in Fig. 12, there is a good agreement between the computational and theoretical results for all segments.

## V. CONCLUSIONS

Axial dispersion of a tracer in a two-dimensional segmented gas-liquid flow is studied computationally using a finite-volume/front-tracking method. The tracer is simulated by a large number of Lagrangian particles, and molecular diffusion is modeled by the random walk of the tracer particles. A perfect elastic collision model is used to treat the boundary conditions for the tracer particles both at the liquid-solid and gas-liquid interfaces. An efficient and robust method is developed for reflecting the tracer particles from

the gas-liquid boundary by utilizing the indicator function that is also used to set the material properties in different phases in the FV/FT method.

The effects of the Peclet number, the capillary number, and segment size are examined. Three different Peclet number regimes are identified and quantified by extensive computational simulations. For small Peclet numbers, the axial dispersion is essentially controlled by convection through the liquid films between the gas bubble and the channel walls, and it becomes independent of the Peclet number in the limit as  $Pe \rightarrow 0$ . On the other hand, when the Peclet number is sufficiently large, the axial dispersion is mainly controlled by the molecular diffusion of the tracer across the boundary between the recirculating bulk region and the film region. In between, there is a transition regime where both the molecular diffusion and convection are important. In the convection-controlled regime, the computational results are found to be in very good agreement with the theory developed by Pedersen and Horvath.<sup>15</sup> For the diffusion-controlled regime, a new model is proposed based on the division of the liquid segment into a film and recirculating regions similar to most of the previous models.<sup>15,20</sup> However, unlike the earlier models, the new model accounts for both the convection and the molecular diffusion and provides explicit dependence on the Peclet and capillary numbers. The model is found to be in reasonably good agreement with the computational results. It is also found that, while the axial mixing is weakly dependent on the capillary number in the diffusion-controlled regime, it depends strongly on the capillary number in the convection-controlled regime. The effects of the length of the liquid slugs on the Peclet number regimes are also examined, and it is found that the three Peclet number regimes are persistent in different segment sizes. Finally, simulations are performed using six bubbles to mimic the bubble-train flows, and the results are found to be in very good agreement with the theory developed by Pedersen and Horvath<sup>15</sup> at low Peclet numbers.

## ACKNOWLEDGMENTS

The first author (M.M.) is partially supported by the Scientific and Technical Research Council of Turkey (TUBITAK) under Grant No. 105M043. We thank the Harvard MRSEC (DMR-0213805). We also thank J. Bird and M. Bazant for helpful conversations.

## APPENDIX: MATHEMATICAL FORMULATION AND NUMERICAL ALGORITHM

### Flow equations

The flow equations are described here in the form suitable for the finite-volume/front-tracking method.<sup>26,32</sup> In the Cartesian coordinates, the two-dimensional incompressible continuity and Navier-Stokes equations can be written in conservation form as

$$\frac{\partial \mathbf{q}}{\partial t} + \frac{\partial \mathbf{f}}{\partial x} + \frac{\partial \mathbf{g}}{\partial y} = \frac{\partial \mathbf{f}_v}{\partial x} + \frac{\partial \mathbf{g}_v}{\partial y} + \mathbf{f}_b, \quad (A1)$$

where



$$\mathbf{q} = \begin{Bmatrix} 0 \\ \rho u \\ \rho v \end{Bmatrix}, \quad \mathbf{f} = \begin{Bmatrix} u \\ \rho u^2 + p \\ \rho uv \end{Bmatrix}, \quad \mathbf{g} = \begin{Bmatrix} v \\ \rho uv \\ \rho v^2 + p \end{Bmatrix}, \quad (\text{A2})$$

and

$$\mathbf{f}_v = \begin{Bmatrix} 0 \\ \tau_{xx} \\ \tau_{xy} \end{Bmatrix}, \quad \mathbf{g}_v = \begin{Bmatrix} 0 \\ \tau_{xy} \\ \tau_{yy} \end{Bmatrix}. \quad (\text{A3})$$

In Eqs. (1)–(3),  $x$  and  $y$  are the Cartesian coordinates and  $t$  is time;  $\rho$ ,  $\mu$ , and  $p$  are the fluid density, the dynamic viscosity, and pressure, respectively, and  $u$  and  $v$  are the velocity components in  $x$  and  $y$  coordinate directions, respectively. The first row in Eq. (1) simply states that the velocity field is solenoidal since the density is taken as constant following a fluid particle, while the last two rows represent the momentum conservation equations in the  $x$  and  $y$  directions, respectively. The viscous stresses appearing in the viscous flux vectors are given by

$$\tau_{xx} = 2\mu \frac{\partial u}{\partial x}, \quad \tau_{yy} = 2\mu \frac{\partial v}{\partial y}, \quad \tau_{xy} = \mu \left( \frac{\partial u}{\partial y} + \frac{\partial v}{\partial x} \right). \quad (\text{A4})$$

The last term in Eq. (1) represents the body forces resulting from surface tension and is given by

$$\mathbf{f}_b = \int_S \sigma \kappa \mathbf{n} \delta(\mathbf{x} - \mathbf{x}^f) ds, \quad (\text{A5})$$

where  $\delta$ ,  $\mathbf{x}^f$ ,  $\sigma$ ,  $\kappa$ ,  $\mathbf{n}$ ,  $S$ , and  $ds$  denote, respectively, the Dirac delta function, the location of the interface, the surface tension coefficient, twice the mean curvature, the outward unit normal vector on the interface, the surface area of the interface, and the surface area element of the interface.

### Tracking the interface

The interface boundary between the drop phase and the ambient fluid are represented by connected Lagrangian marker points moving with the local flow velocity interpolated from the neighboring curvilinear grid points. The communication between the curvilinear grid and the interface marker points is maintained efficiently using an auxiliary regular Cartesian grid cast on the curvilinear grid.<sup>26</sup> An indicator function is defined such that it is unity inside the droplet and zero outside. Based on the locations of the interface marker points, unit magnitude jumps are distributed in a conservative manner on the regular grid points near the interface and are integrated to compute the indicator function everywhere. This procedure involves solution of a separable Poisson equation on a regular grid and yields a smooth transition of the indicator function across the interface. The indicator function is then interpolated from the regular Cartesian grid onto the curvilinear grid using bilinear interpolations. Once the indicator function distribution is determined, the material properties such as viscosity, density, and molecular diffusivity are set as a function of the indicator function. The interface marker points are also used to compute the surface tension forces at the interface, which are then distributed on the neighboring curvilinear grid cells in a conservative manner

and added to the discrete momentum equations as source terms. The details of the FV/FT method can be found in Refs. 26 and 32.

### Tracer particles

A large number of passive tracer particles are used to visualize and quantify mixing in the continuous fluid. The molecular mixing is modeled by a random walk of tracer particles. Using a Lagrangian description, the location of the  $m$ th tracer particle  $\mathbf{X}_m$  evolves by

$$d\mathbf{X}_{m_i} = \mathbf{U}_{m_i} dt + \sqrt{2D} d\mathbf{W}_i, \quad (\text{A6})$$

where  $\mathbf{U}_m$  is the mean velocity interpolated from the Eulerian curvilinear grid onto the location of the marker point,  $dt$  is the time increment,  $D$  is the molecular diffusion coefficient for the tracer, and  $d\mathbf{W}$  is a vector valued Wiener process<sup>33</sup> with properties  $\langle d\mathbf{W} \rangle = 0$  and  $\langle d\mathbf{W}_i d\mathbf{W}_j \rangle = \delta_{ij} dt$ , where  $\langle \cdot \rangle$  denotes the mean and  $\delta_{ij}$  is the Kronecker delta. Equation (A6) is approximated using a predictor-corrector method and is solved together with the flow equations. In the first step, the locations of tracer particles are predicted using an explicit Euler method as

$$\mathbf{X}_{m_i}^* = \mathbf{X}_{m_i}^n + \mathbf{U}_{m_i}^n \Delta t + \sqrt{2D\Delta t} \xi_i^{(1)}, \quad (\text{A7})$$

where superscripts  $n$  denote the  $n$ th time level and  $\xi_i^{(1)}$  is a normally distributed random number. Second, the flow equations are integrated in time using the FV/FT method. Finally, the locations of the tracer particles are corrected as

$$\mathbf{X}_{m_i}^{n+1} = \mathbf{X}_{m_i}^n + \frac{1}{2}(\mathbf{U}_{m_i}^n + \mathbf{U}_{m_i}^*) \Delta t + \sqrt{2D\Delta t} \xi_i^{(2)}, \quad (\text{A8})$$

where  $\xi_i^{(2)}$  is an independent random number and  $\mathbf{U}^*$  is the velocity interpolated from the velocity field  $\mathbf{U}^{n+1}$  onto the predicted particle locations  $\mathbf{X}^*$ . The method is weak second-order accurate in time. Note that the particle tracking and interpolation schemes employed for the tracer particles are the same as those used for the Lagrangian marker points in the FV/FT method.<sup>26</sup>

The tracer particles may cross the channel walls as well as the gas-liquid interface mainly due to the random walk and also due to numerical errors. Any particles crossing the boundaries are reflected assuming a perfect reflection as sketched in Fig. 13. Although the reflection from the channel walls is straightforward, it is not easy to reflect the tracer particles from the gas-liquid boundary since a straightforward reflection is computationally too expensive, especially when a large number of tracer particles is used in the simulations at low Peclet numbers. To circumvent this difficulty, the indicator function is utilized to determine the tracer particles that have crossed the gas-liquid interface as well as to reflect them from the interface. The indicator function is denoted by  $I$  and is the same as the one computed in the FV/FT method in order to set the material properties smoothly inside and outside of the bubbles. As mentioned before, the indicator function is zero outside of the bubble and is unity inside the bubble. The width of the transition layer is approximately four grid sizes and the contour line of  $I=0.5$  is a very good approximation to the location of the interface. The

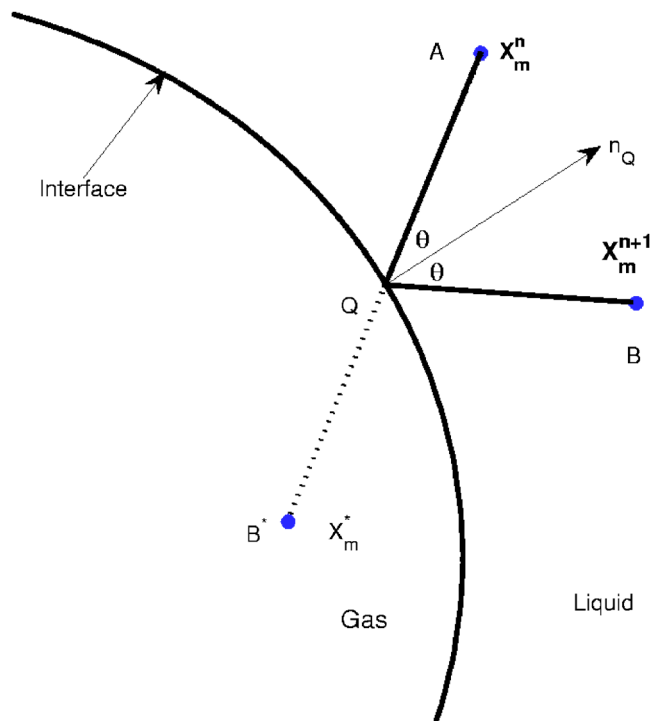


FIG. 13. (Color online) Reflection of tracer particles crossing the gas-liquid interface.

boundary conditions at the gas-liquid and liquid-wall interfaces are applied both at the predictor and corrector steps, but the procedure is explained here only for a single explicit Euler step. In advancing the location of the  $m$ th tracer particle from time level  $n$  to time level  $n+1$  using a single explicit Euler method, we assume that the tracer particle initially resides in the liquid phase, i.e.,  $I(\mathbf{X}_m^n) < 0.5$ , where  $I(\mathbf{X}_m^n)$  denotes the value of the indicator function interpolated on the particle location  $\mathbf{X}_m^n$ , and it moves to the location  $\mathbf{X}_m^*$ . It is assumed that the particle has not crossed the gas-liquid interface if  $I(\mathbf{X}_m^*) \leq 0.5$  and the particle location is updated as  $\mathbf{X}_m^{n+1} = \mathbf{X}_m^*$ . Otherwise the particle has crossed the interface and is reflected from the interface as follows. The distance between the initial particle location  $\mathbf{X}_m^n$  and the location where the particle has crossed the interface  $\mathbf{X}_Q$  is computed by using a simple interpolation scheme based on the indicator function as

$$|AQ| = \frac{0.5 - I_m^n}{\max(\epsilon_I, I_m^* - I_m^n)} |AB^*|, \quad (\text{A9})$$

where, for instance,  $I_m^n$  is the value of the indicator function interpolated onto the location  $\mathbf{X}_m^n$  and  $\epsilon_I$  is a small number taken as  $\epsilon_I = 0.01$  in the present study. Then  $\mathbf{X}_Q$  is computed as

$$\mathbf{X}_Q = \mathbf{X}_m^n + |AQ|\mathbf{v}, \quad (\text{A10})$$

where  $\mathbf{v} = \vec{AB^*}/|AB^*|$ . The unit normal vector at the interface is approximated as

$$\mathbf{n} = -\frac{\nabla I}{|\nabla I|}. \quad (\text{A11})$$

In the present implementation, the normal vectors are first computed at all four vertices of the regular grid cell surrounding the intersection point  $Q$  by using central differences and a bilinear interpolation is used to compute the normal vector  $\mathbf{n}_Q$  at point  $Q$ . Finally,  $\mathbf{X}_m^{n+1}$  is computed by a perfect reflection about the normal vector  $\mathbf{n}_Q$  as

$$\mathbf{X}_m^{n+1} = \mathbf{X}_Q - [2(\mathbf{v} \cdot \mathbf{n}_Q)\mathbf{n}_Q - \mathbf{v}][QB^*]. \quad (\text{A12})$$

This procedure is found to be very robust even for the cases of very large molecular diffusivities, e.g., Peclet numbers as small as 10. However, some tracer particles may still escape into the gas bubble due to numerical errors mainly arising from Lagrangian grid restructuring,<sup>27</sup> and such particles are simply disregarded in the present study. We emphasize here that the total number of disregarded particles was found to be less than 1% throughout the simulations in all of the results presented in this paper.

<sup>1</sup>G. Bercic and A. Pintar, "The role of gas bubbles and liquid slug length on mass transport in the Taylor flow through capillaries," *Chem. Eng. Sci.* **52**, 3709 (1997).

<sup>2</sup>S. Iradoust and B. Andersson, "Mass-transfer and liquid-phase reaction in a segmented two-phase flow monolithic catalyst reactor," *Chem. Eng. Sci.* **43**, 1983 (1988).

<sup>3</sup>M. T. Kreutzer, F. Kapteijn, J. A. Moulijn, and J. J. Heiszwolf, "Multiphase monolith reactors: Chemical reaction engineering of segmented flow in microchannels," *Chem. Eng. Sci.* **60**, 5895 (2005).

<sup>4</sup>R. H. Patrick, T. Klindera, L. L. Crynes, R. L. Cerro, and M. A. Abraham, "Residence time distribution in 3-phase monolith reactor," *AIChE J.* **41**, 649 (1995).

<sup>5</sup>B. K. Paul and S. P. Moulik, "Microemulsions: An overview," *J. Dispersion Sci. Technol.* **18**, 301 (1997).

<sup>6</sup>L. T. Skeggs, "An automatic method for colorimetric analysis," *Am. J. Clin. Pathol.* **28**, 311 (1957).

<sup>7</sup>L. R. Snyder and H. J. Adler, "Dispersion in segmented flow through glass tubing in continuous-flow analysis—Ideal model," *Anal. Chem.* **48**, 1017 (1976).

<sup>8</sup>L. R. Snyder and H. J. Adler, "Dispersion in segmented flow through glass tubing in continuous-flow analysis—Nonideal model," *Anal. Chem.* **48**, 1022 (1976).

<sup>9</sup>A. Günther, S. A. Khan, M. Thalmann, F. Trachsel, and K. F. Jensen, "Transport and reaction in microscale segmented gas-liquid flow," *Lab Chip* **4**, 278 (2004).

<sup>10</sup>G. I. Taylor, "Deposition of viscous fluid on the wall of a tube," *J. Fluid Mech.* **10**, 161 (1961).

<sup>11</sup>F. P. Bretherton, "The motion of long bubbles in tubes," *J. Fluid Mech.* **10**, 166 (1961).

<sup>12</sup>P. Aussillous and D. Quere, "Quick deposition of a fluid on the wall of a tube," *Phys. Fluids* **12**, 2367 (2000).

<sup>13</sup>M. Muradoglu and H. A. Stone, "Mixing in a drop moving through a serpentine channel: A computational study," *Phys. Fluids* **17**, 073305 (2005).

<sup>14</sup>M. Muradoglu and H. A. Stone, "Motion of large bubbles in curved channels," *J. Fluid Mech.* **570**, 455 (2007).

<sup>15</sup>H. Pedersen and C. Horvath, "Axial dispersion in a segmented gas-liquid flow," *Ind. Eng. Chem. Fundam.* **20**, 181 (1981).

<sup>16</sup>A. Günther and K. F. Jensen, "Multiphase microfluidics: from flow characteristics to chemical and material synthesis," *Lab Chip* **6**, 1487 (2006).

<sup>17</sup>M. P. Dudukovic, F. Larachi, and P. L. Mills, "Multiphase catalytic reactors: A perspective on current knowledge and future trends," *Catal. Rev.-Sci. Eng.* **44**, 123 (2002).

<sup>18</sup>M. T. Kreutzer, J. J. W. Bakker, F. Kapteijn, J. A. Moulijn, and P. J. T. Verheijen, "Scaling-up multiphase monolith reactors: Linking residence time distribution and feed maldistribution," *Ind. Eng. Chem. Res.* **44**, 4898 (2005).

- <sup>19</sup>T. C. Thulasidas, M. A. Abraham, and R. L. Cerro, "Dispersion during bubble-train flow in capillaries," *Chem. Eng. Sci.* **54**, 61 (1999).
- <sup>20</sup>T. C. Thulasidas, M. A. Abraham, and R. L. Cerro, "Flow patterns in liquid slugs during bubble-train flow inside capillaries," *Chem. Eng. Sci.* **52**, 2947 (1997).
- <sup>21</sup>A. Günther, M. Jhunjhunwala, M. Thalmann, M. A. Schmidt, and K. F. Jensen, "Micromixing of miscible liquids in segmented gas-liquid flow," *Langmuir* **21**, 1547 (2005).
- <sup>22</sup>B. K. H. Yen, A. Günther, M. A. Schmidt, K. F. Jensen and M. G. Bawendi, "A microfabricated gas-liquid segmented flow reactor for high-temperature synthesis: The case of CdSe quantum dots," *Angew. Chem., Int. Ed.* **44**, 5447 (2005).
- <sup>23</sup>W. Salman, A. Gavriilidis, and P. Angeli, "A model for predicting axial mixing during gas-liquid Taylor flow in microchannels at low Bodenstein numbers," *Chem. Eng. J.* **101**, 391 (2004).
- <sup>24</sup>W. Salman, A. Gavriilidis, and P. Angeli, "Sample pulse broadening in Taylor flow microchannels for screening applications," *Chem. Eng. Technol.* **28**, 509 (2005).
- <sup>25</sup>F. Trachsel, A. Günther, S. Khan, and K. F. Jensen, "Measurement of residence time distribution in microfluidic systems," *Chem. Eng. Sci.* **60**, 5729 (2005).
- <sup>26</sup>M. Muradoglu and A. D. Kayaalp, "An auxiliary grid method for computations of multiphase flows in complex geometries," *J. Comput. Phys.* **214**, 858 (2006).
- <sup>27</sup>G. Tryggvason, B. Bunner, A. Esmaeeli, D. Juric, N. Al-Rawahi, W. Tauber, J. Han, S. Nas, and Y.-J. Jan, "A front-tracking method for the computations of multiphase flow," *J. Comput. Phys.* **169**, 708 (2001).
- <sup>28</sup>S. O. Unverdi and G. Tryggvason, "A front-tracking method for viscous, incompressible flows," *J. Comput. Phys.* **100**, 25 (1992).
- <sup>29</sup>D. A. Caughey, "Implicit multigrid computation of unsteady flows past cylinders of square cross-section," *Comput. Fluids* **30**, 939 (2001).
- <sup>30</sup>M. A. Leveque, "Les lois de la transmission de chaleur par convection," *Ann. Mines* **13**, 201 (1928).
- <sup>31</sup>H. A. Stone, "Heat mass-transfer from surface-films to shear flows at arbitrary Peclet numbers," *Phys. Fluids A* **1**, 1112 (1989).
- <sup>32</sup>M. Muradoglu and S. Gokaltun, "Implicit multigrid computations of buoyant drops through sinusoidal constrictions," *J. Appl. Mech.* **71**, 1 (2004).
- <sup>33</sup>S. B. Pope, *Turbulent Flows* (Cambridge University Press, Cambridge, UK, 2000).